

## Article

# The Magnetic Properties and Photoactivity of Bi-Magnetic Nanostructures for Hydrogen Production

Hind Alsnani <sup>1</sup>, Manal M. Khowdiary <sup>2</sup>  and Mohamed S. A. Darwish <sup>3,\*</sup> 

<sup>1</sup> Physics Department, Lieth University Collage, Umm el Qura University, Mecca 2207, Saudi Arabia; hasnani@uqu.edu.sa

<sup>2</sup> Chemistry Department, Lieth University Collage, Umm el Qura University, Mecca 2207, Saudi Arabia; mmkhowdiary@uqu.edu.sa

<sup>3</sup> Egyptian Petroleum Research Institute, 1 Ahmed El-Zomor Street, El Zohour Region, Nasr City, Cairo 11727, Egypt

\* Correspondence: msa.darwish@gmail.com

**Abstract:** The major challenge of hydrogen production via photocatalytic water-splitting is to utilize active photocatalysts that respond to a wide range of visible light. In this work, hybrid nanostructures purposed to combine the tunable magnetic behavior of soft/semi-hard magnetic particles have shown advantageous photoactivity. A series of photocatalysts based on ferrite nanoparticles, magnetite nanoparticles (MNPs), cobalt ferrite nanoparticles (CFNPs), magnetite nanoparticles coated on cobalt ferrite nanoparticles (MNPs @ CFNPs), and cobalt ferrite nanoparticles coated on magnetite nanoparticles (CFNPs @ MNPs) were prepared. The size, morphology, magnetic properties, and optical activity of the prepared nanoparticles were characterized using multiple techniques. CFNPs @ MNPs had the largest particle size (~14 nm), while CFNPs had the smallest (~8 nm). The saturation magnetization of CFNPs @ MNPs was the highest at 55.45 emu g<sup>-1</sup>. The hydrogen yield was 60, 26, 3.8, and 93 mmole min<sup>-1</sup> g<sup>-1</sup> for MNPs, CFNPs, MNPs @ CFNPs, and CFNPs @ MNPs. CFNPs @ MNPs displayed a superior photocatalytic performance for hydrogen production under the magnetic force as appropriate materials for water-splitting processing.

**Keywords:** bi-magnetic; ferrite; hydrogen production; nanostructure; photocatalysts



**Citation:** Alsnani, H.; Khowdiary, M.M.; Darwish, M.S.A. The Magnetic Properties and Photoactivity of Bi-Magnetic Nanostructures for Hydrogen Production. *Crystals* **2023**, *13*, 1527. <https://doi.org/10.3390/cryst13101527>

Academic Editors: Lizhu Ren and Xuecheng Sun

Received: 25 September 2023

Revised: 14 October 2023

Accepted: 19 October 2023

Published: 22 October 2023



**Copyright:** © 2023 by the authors. Licensee MDPI, Basel, Switzerland. This article is an open access article distributed under the terms and conditions of the Creative Commons Attribution (CC BY) license (<https://creativecommons.org/licenses/by/4.0/>).

## 1. Introduction

The primary demand for society is the production of renewable and clean energy [1–8]. Recently, hydrogen production has received a lot of interest due to its high energy content and clean energy source. Different techniques have been used for hydrogen production [2–5]. However, considering the simplicity of the technique and the lower required energy, utilizing a photocatalytic through a water-splitting technique is an alternative to other methods [3,4]. Ferrite nanoparticles with the general formula  $M\text{-Fe}_2\text{O}_4$  have been considered attractive with their unique construction and unparalleled magnetic character. The magnetic ferrite catalysts can be prepared by using different techniques such as sol–gel, coprecipitation, and hydrothermal techniques [9–13]. Among them, the coprecipitation technique is a favorable method due to it being cost-effective, simple, environmentally friendly, and amenable to operation at relatively low temperatures. It produces no hazardous intermediates or solvents, requires no precursor complexes, and has the ability to be scaled up. Cobalt ferrite ( $\text{CoFe}_2\text{O}_4$ ) is of considerable attentiveness because of its excellent magneto-crystalline anisotropy with photo stability [14–16]. As the nanoparticle size decreases, the magnetization behavior of the particle enormously decreases. Using bi-magnetic nanoparticles as photocatalysts is favorable in a water-splitting technique. The inner-magnetic character of the photocatalyst can improve the hydrogen yields. The existence of two oxide types (soft and semi-hard

magnetic nanoparticles) in the photocatalyst structure is extraordinary due to the presence of oxygen vacancies in the structures [17–26]. The shape of MNP structures, like spherical, rod-shaped, or cubic, can vary greatly because it expands the scope of their applications [23,24]. In particular, spherical MNPs are the most promising magnetically controlled systems in fundamental and applied research. The spherical shape structures and particle sizes can significantly tune its magnetic-photo behavior. The covering of the magnetite nanoparticles of  $\text{Fe}_3\text{O}_4$  (soft magnetic nanoparticles) with cobalt ferrite nanoparticles (semi-hard magnetic nanoparticles) using the coprecipitation method can enhance the photocatalytic activity of the nanoparticles in hydrogen production. This suggests that  $\text{CoFe}_2\text{O}_4$  on the  $\text{Fe}_3\text{O}_4$  is active as an electron catch for the electrons leaving to  $\text{Fe}_3\text{O}_4$  which prohibits the regrouping of the hole and the electrons. It likely assists the photocatalytic efficiency by widening the reaction area on the  $\text{Fe}_3\text{O}_4$  and expanding the electron's existence [27–30]. In addition, a magnetic field can enhance the photocatalytic reaction by raising the carrier movement and lowering the recombination of light-induced hot-charge carriers.

In our previous work, we studied the influence of magnetic force on magnetic photocatalyst nanostructures based on three types of element oxides (Fe, Zn, Co) [31]. Zinc cobalt ferrite nanoparticles coated onto magnetite nanoparticles (ZCFNPs @ MNPs) showed a low hydrogen yield with only  $1.4 \text{ mmole min}^{-1} \text{ g}^{-1}$ . This may result from the high band gap energy of this nanostructure [31]. In this work, we attempt to have a bi-magnetic nanostructure as a photocatalyst with lower band gap energy. The proposed nanostructure is composed of only two types of element oxides (Fe, Co), a soft magnetic phase, and a semi-hard magnetic phase. The high hydrogen yield was  $93 \text{ mmole min}^{-1} \text{ g}^{-1}$  for CFNPs @ MNPs. The lowest band gap value (1.4 eV) of CFNPs @ MNPs enhanced the photocatalytic activity of this structure by reducing the light irradiation required through the splitting reaction. The current work continues the previously established attempts and has shown improvement in investigating photocatalysts for hydrogen production.

## 2. Materials and Methods

### 2.1. Materials

Iron (III) chloride hexahydrate ( $\text{FeCl}_3 \cdot 6\text{H}_2\text{O}$ ,  $\geq 99\%$ ), iron (II) chloride tetrahydrate ( $\text{FeCl}_2 \cdot 4\text{H}_2\text{O}$ ,  $\geq 99\%$ ), Cobalt(II) chloride hexahydrate ( $\text{CoCl}_2 \cdot 6\text{H}_2\text{O}$ ,  $\geq 98\%$ ), and ammonium hydroxide (30%  $\text{NH}_3$  in  $\text{H}_2\text{O}$ ) were ordered from Sigma Aldrich (St. Louis, MO, USA).

### 2.2. Fabrication of Bi-Magnetic Nanostructure

Bi-magnetic nanostructures were synthesized using the coprecipitation method (Table 1). This technique is an altered method of the already discussed coprecipitation process [31]. Precursors were dissolved in 50 mL of distilled water and mixed well for 15 min to obtain a homogeneous solution. The temperature was then increased to  $60^\circ\text{C}$  and maintained for 5 min to ensure complete homogenous mixing. With vigorous stirring, 20 mL of ammonium hydroxide (30%) was added in a dropwise manner to induce particle growth, followed by additional stirring for 30 min at  $60^\circ\text{C}$  to evaporate any excess ammonia. The black precipitate was washed several times using distilled water to remove possible impurities (e.g., ammonium salts). Magnetic nanoparticles were separated from the medium using a magnetic bar. The products were then dried for 24 h. The second step involved coating the prepared core with a shell layer, and the same procedure described above was employed with the addition of the shell precursors described in Table 1.

**Table 1.** Bi-magnetic nanostructure preparation.

Nanostructure	Core	Shell and Precursors					
		Layer	Fe <sup>+3</sup> (Mole)	Fe <sup>+2</sup> (Mole)	DW (mL)	Co <sup>+2</sup> (Mole)	Amm. (mL)
MNPs	Fe <sub>3</sub> O <sub>4</sub>	-	0.590	0.399	50	-	20
CFNPs	CoFe <sub>2</sub> O <sub>4</sub>	-	0.590	0.399	50	0.199	20
MNPs @ CFNPs	CoFe <sub>2</sub> O <sub>4</sub> (0.3 g)	Fe <sub>3</sub> O <sub>4</sub>	0.149	0.098	25	-	5
CFNPs @ MNPs	Fe <sub>3</sub> O <sub>4</sub> (0.3 g)	CoFe <sub>2</sub> O <sub>4</sub>	0.074	0.049	50	0.024	5

### 2.3. Hydrogen Production System

The hydrogen production system, which was utilized in this research, is described in our earlier work. A certain amount of the prepared catalysts (0.5 g) was added, on a separate basis, to the water–methanol mixture (1:1 by weight). The production system was first degassed through the purging of pure nitrogen for 15 min. Then, the system was subjected to vigorous stirring (600 rpm) while being exposed to a visible light spectrum (linear halogen lamp has a wavelength = 550 nm) of a power equal to 500 W. A radiation power intensity of 0.13 W/mL was generated inside the reaction system. The hydrogen generation experiments were next completed at ambient temperature for 45 min. At the end of each experiment, the produced gas was gathered and evaluated using gas chromatography methodology. The hydrogen production procedures were performed in triplicate to verify the consistency of the acquired results.

### 2.4. Characterizations

X-ray diffraction (XRD) of the MFNs was analyzed using an X-ray diffractometer (Rigaku, Tokyo, Japan) equipped with a copper X-ray tube and Cu K $\alpha$  radiation. The measurements were performed at a scan speed of 4°/min with a 2 $\theta$  ranging from 25° to 65°. Zeta potential measurements were performed using the zeta-potential and particle size analyzer (ELSZ-2000; Photal Otsuka Electronics, Osaka, Japan). For zeta potential measurements, a ferrofluid at a concentration of 8.3 mg/mL and a pH range of 3.5–5 was used. UV spectroscopic analysis of the materials was measured using a UV-spectrophotometer (V-570, JASCO, Japan). The clear colloid obtained after sonicating the nanoparticles dispersed in deionized water was used for measurement and pure deionized water was used as a reference. The magnetic properties of the samples were measured using a vibrating sample magnetometer (VSM; Lake Shore 7400 series; Lake Shore Cryotronics, Westerville, OH, USA). The metal contents of the materials were analyzed using inductively coupled plasma–optical emission spectroscopy (ICP-OES; Optima 8300, PerkinElmer, Waltham, MA, USA). A total of 0.1 g of the nanoparticles dispersed in 25 mL of D.I. water was subjected to ultrasound before the analyses. The quantitation range for the cost elements was 50 ppm for ICP-OES. The samples were made using an aqueous nitric acid solution. Additional dilutions were performed to make the sample concentrations according to the specified range. The morphology and size of the materials were characterized using transmission electron microscopy (TEM) (JEM-2100 LaB6, JEOL, Akishima, Tokyo, Japan) at 200 keV.

## 3. Results and Discussion

### 3.1. Nanostructures Synthesis

Tuning the structure of the prepared materials plays a definite role in magnetic and optical properties, which is important for improving the photoactivity of the nanostructures. Bi-magnetic nanostructures, i.e., MNPs @ CFNPs and CFNPs @ MNPs, were prepared via coprecipitation techniques. It included a two-step preparation technique where the prepared NPs were utilized as cores for the subsequent precipitation of the coated layer, as

illustrated in Figure 1. The prepared photocatalyst was recoverable from the reaction by using magnetic separation by a magnet bar (Figure 1).

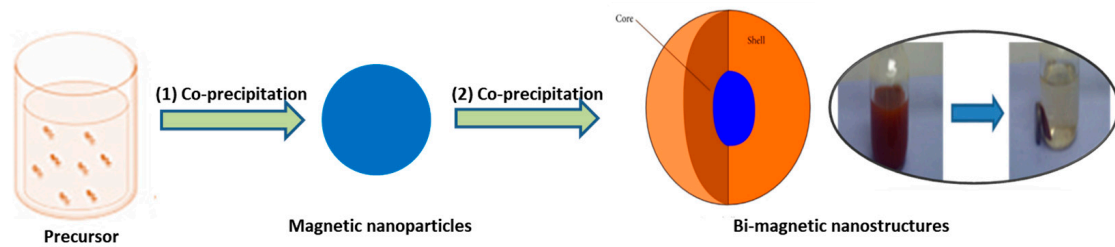


**Figure 1.** Preparation of bi-magnetic nanostructures.

### 3.2. Characterizations of the Nanostructure

The morphology and size of the nanostructures were investigated via TEM (Figure 2). They exhibited poly-disperse characteristics with the tendency to group as a result of the high surface energy. CFNPs @ MNPs had the largest particle size (~14 nm), while CFNPs had the smallest size (~8 nm) (Table 2).

**Table 2.** The size and zeta potential of the particles.

Properties / Sample	MNPs	CFNPs	MNPs @ CFNPs	CFNPs @ MNPs
Size (nm) from XRD	9.8	8.7	11.1	9.4
Size (nm) from TEM	10 ± 0.3	8 ± 2.0	12 ± 1.7	14 ± 0.5
Zeta potential (mV)	-2.9 ± 0.6	-30.4 ± 0.5	-29.6 ± 0.9	-26.0 ± 0.6

The magnetite phase and size were investigated via XRD. The indexed peaks (440), (511), (422), (400), (311), and (220) lattice planes matched the standard pattern (JCPDS data (#221086)) for the dominant  $\text{Fe}_3\text{O}_4$ . However, the indexed peaks (104), (113), (116), and (024) planes matched  $\alpha\text{-Fe}_2\text{O}_3$  (Figure 3). In the presence of atmospheric conditions with a lack of oxygen encapsulation prevention, the  $\text{Fe}_3\text{O}_4$  phase was oxidized, i.e.,  $\text{Fe}_3\text{O}_4 \rightarrow \text{Fe}_2\text{O}_3$  and also  $\text{Fe}_2\text{O}_3$  coming from  $\text{CoFe}_2\text{O}_4$  [32]. The crystallite sizes of the prepared nanostructures were studied by XRD. The size was calculated using the broadening of the maximum intensity peak (Table 2) according to the Scherrer equation:

$$\text{Crystallite size} = K\lambda / (B\cos\theta) \quad (1)$$

where B is the full-width at half-maximum (FWHM) of the XRD peak,  $\lambda$  is the X-ray wavelength (1.5406 Å), K is the Scherrer constant (shape parameter, 0.89), and  $\theta$  is the XRD peak position.

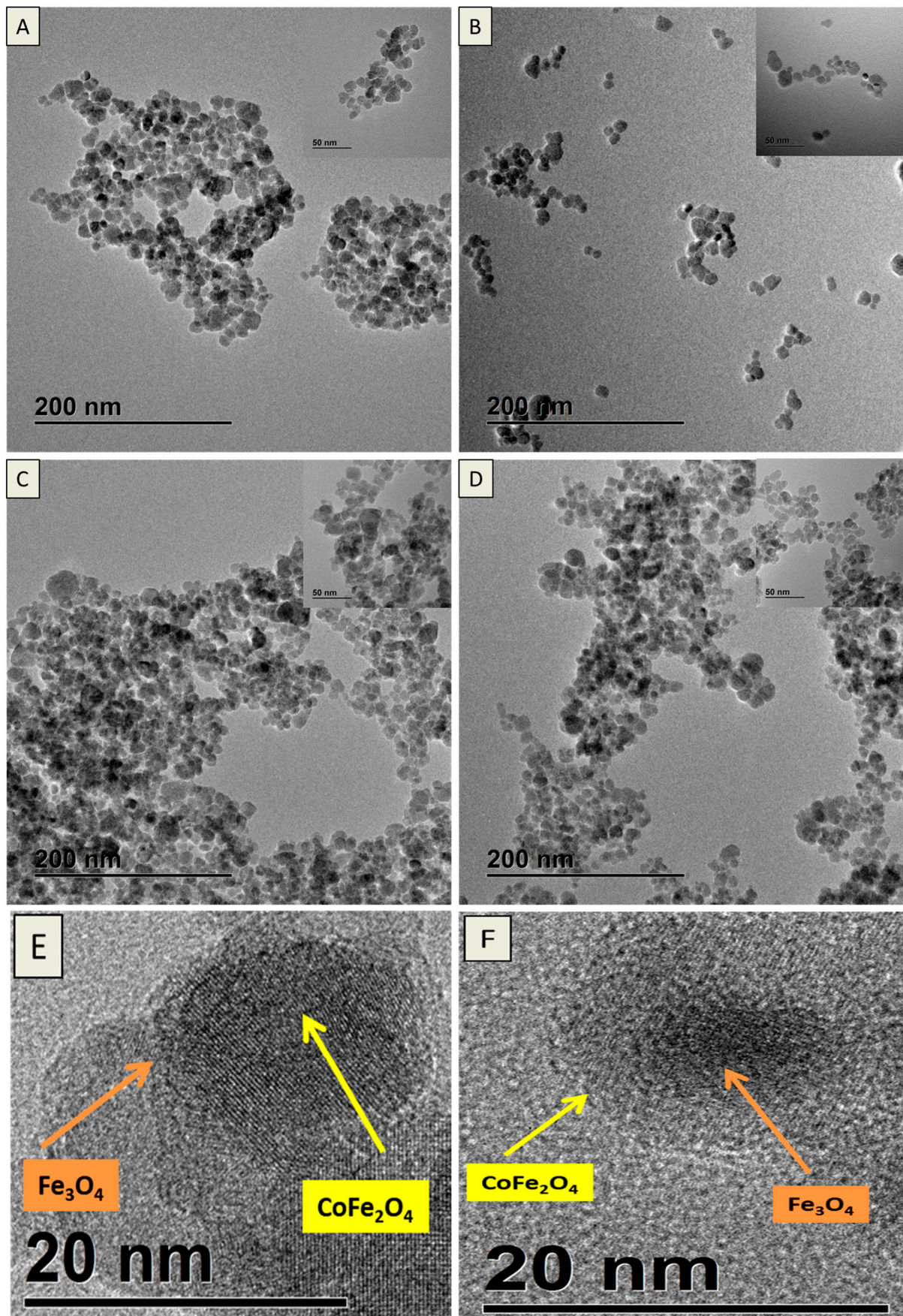
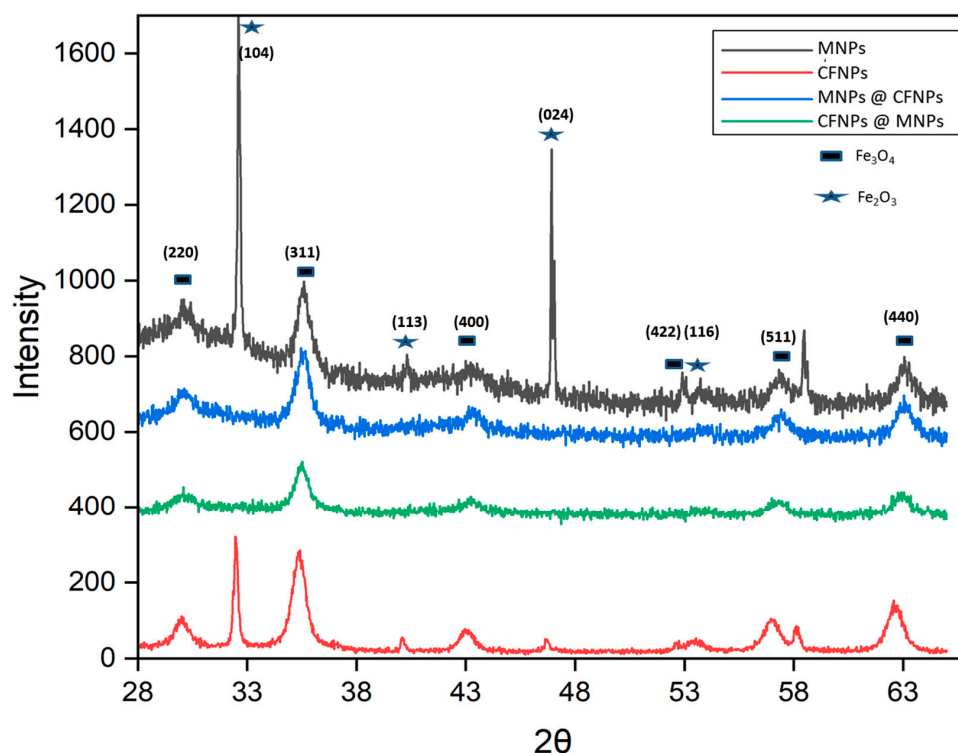


Figure 2. TEM of (A) MNPs (B) CFNPs, (C,E) MNPs @ CFNPs, and (D,F) CFNPs @ MNPs.



**Figure 3.** XRD of MNPs, CFNPs, MNPs @ CFNPs, and CFNPs @ MNPs.

The broadening of the peaks depended on different factors like instrumental effects and strain effects. The peaks were to some extent broadening and weak, probably as a result of disorder and small crystallite effects. MNPs @ CFNPs had the largest crystallite size (~11 nm), while CFNPs had the smallest (~8 nm). The size increased with a decrease in the lattice parameter (8.38 Å) for MNPs @ CFNPs by the amorphous layer presence of FeO coating the core or a partial dissolution of the core.

Zeta potential ( $\zeta$ ) was studied as it is associated with colloidal solution stability (Figure 4). Nanostructure stabilization is remarkable for its application [33,34]. The used photocatalysts should be stable, inexpensive, and have light absorbers fit to create photons with enough ability for the splitting process. The  $\zeta$  values for CFNPs and MNPs were  $-30.4 \pm 0.5$  and  $-2.9 \pm 0.6$  mV, respectively (Table 2). The lower value revealed that the material may exhibit low stability in the solution. The lower  $\zeta$  value (0 to  $\pm 5$  mV) increased the Van der Waals inter-particle attraction, and rapid aggregation occurred. The high value of the zeta potential proposes that the particles will be more stable due to an elevated electrostatic repulsion force. The higher value of the zeta potential with about  $\pm 30$  mV was the limiting value region of the high colloidal stability. The metal contents for the prepared nanostructures were detected via ICP-OES. It was observed that the highest and lowest iron content in MNPs @ CFNPs and MNPs was 68.6 and 50.8%, respectively. The highest and lowest cobalt content was detected in CFNPs @ MNPs and MNPs @ CFNPs at 8.48 and 2.83%, respectively, which is expected to influence their behavior. The difference in the cobalt content between CFNPs@MNPs and MNPs@CFNPs may occur as a result of the partial dissolution of the core with the formation of the coating layer.

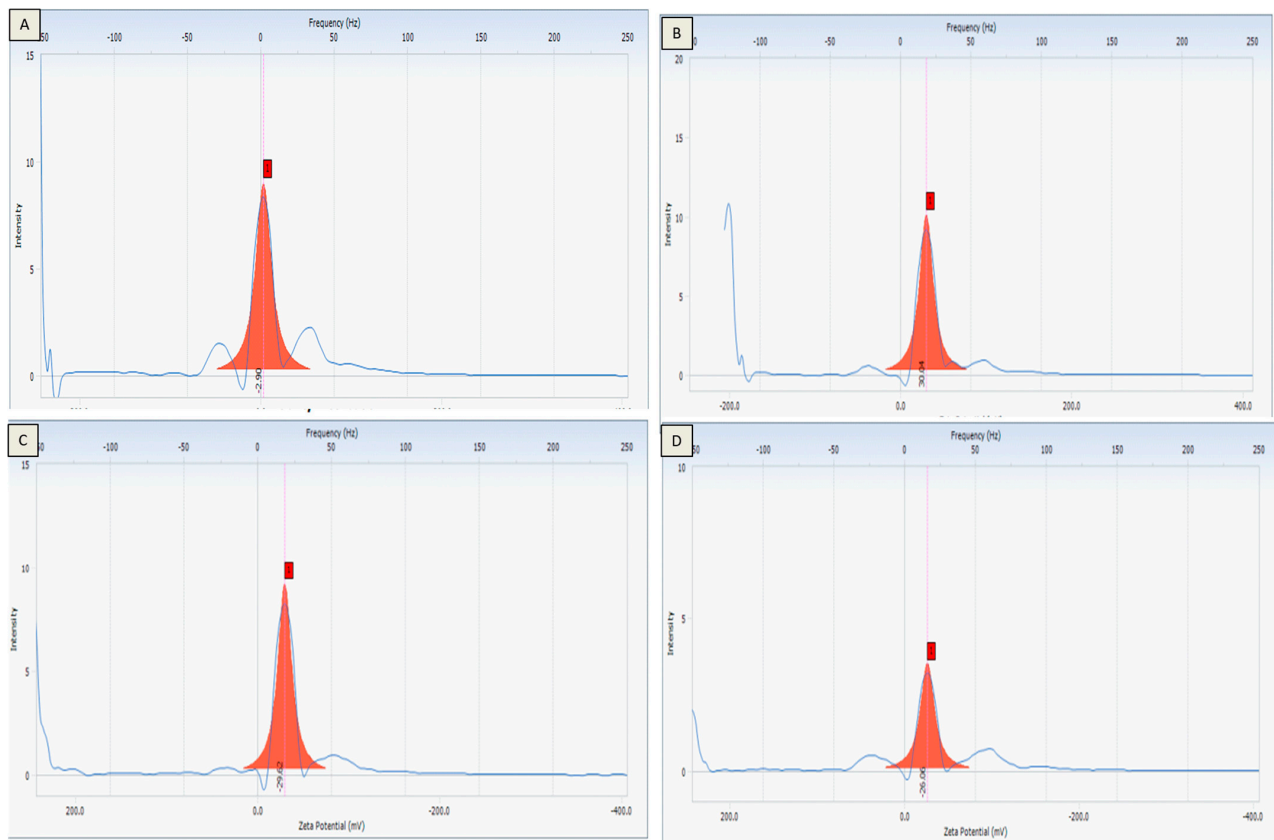


**Figure 4.** Zeta potential of (A) MNPs (B) CFNPs, (C) MNPs @ CFNPs, and (D) CFNPs @ MNPs.

### 3.3. Magnetic Properties of the Nanostructures

The magnetic character could be investigated using VSM, SQUID, or magnetic force microscopy to measure magnetic signals [35,36]. VSM is a more versatile, cost-effective technique that does not require cryo-temperatures like SQUID and is capable of detecting ultra-small magnetic moments in contrast to magnetic force microscopy. The magnetic character of the nanostructure was investigated via VSM at room temperature. The M-H plot exhibited hysteresis loops for the prepared nanostructure (Figure 5). This confirmed the ferromagnetism behavior of the particles. The magnetic values of the coercivity ( $H_c$ ), remanent magnetization ( $M_r$ ), saturation magnetizations ( $M_s$ ), and the squareness values of the hysteresis loops were recorded (Table 3). The prepared MNPs showed a low  $H_c$  of 40.5 Oe. CFNPs @ MNPs showed the highest  $M_s$  with a low  $M_r$  at 55.4 and 5.0  $\text{emu g}^{-1}$ , respectively. Retention is key to recovery. Nanostructures intended to combine the beneficial properties of soft/semi-hard magnetic particles have shown remarkable magnetic character. The  $H_c$  value of CFNPs @ MNPs exists between the core and shell values [37]. The  $M_s$  value of the nanostructure (CFNPs @ MNPs) was enhanced to the core MNP value [38]. The  $M_s$  of the nanostructure (MNPs @ CFNPs) was decreased to the core CFNP value. This may be due to the magnetic value varying with the morphology and size of the particle until beyond a critical size when the magnetization is steady and becomes almost equal to the bulk value. The  $M_s$  was low with the existence of a magnetite soft layer in MNPs @ CFNPs when compared to the reversed nanostructure of CFNPs @ MNPs. The lower magnetization value is the result of the disorder in the crystalline nanostructure with a small magnetic domain, or the rise in the oxidation degree and non-magnetic content [39]. The critical size for the ferromagnetic  $\text{CoFe}_2\text{O}_4$  via the size tuned (4.2–4.8 nm) and the magnetization ( $M_s$  26–30  $\text{emu g}^{-1}$ ) was recorded by Pereira et al. [40]. The coercivity of the nanostructures ( $\text{CoFe}_2\text{O}_4$ @ $\text{MnFe}_2\text{O}_4$  and  $\text{MnFe}_2\text{O}_4$ @ $\text{CoFe}_2\text{O}_4$ ) with changing core and shell volume proportions was modulated [41]. The magnetic character of the nanostructure

was planned as a function of the volume proportion of the magnetic phase kind. The high  $M_s$  is important for a practical photocatalytic hydrogen production application. When removing the magnetic field, the photocatalysts should not have any residual magnetism property to avoid the collection of recycled photocatalysts for the next hydrogen production cycle. These photocatalysts can be separated easily from the system by a magnetic bar. Meanwhile, the recycled nanoparticles can be re-dispersed for further hydrogen production experiments. The reduced remanence (SQ) is  $M_r/M_s$ . When the SQ value is  $\geq 0.5$ , the particles pose a single magnetic domain structure, while an SQ value of  $< 0.5$  poses a multi-domain structure. In this study, the SQ value was  $< 0.5$ , proposing the presence of a multi-domain structure.

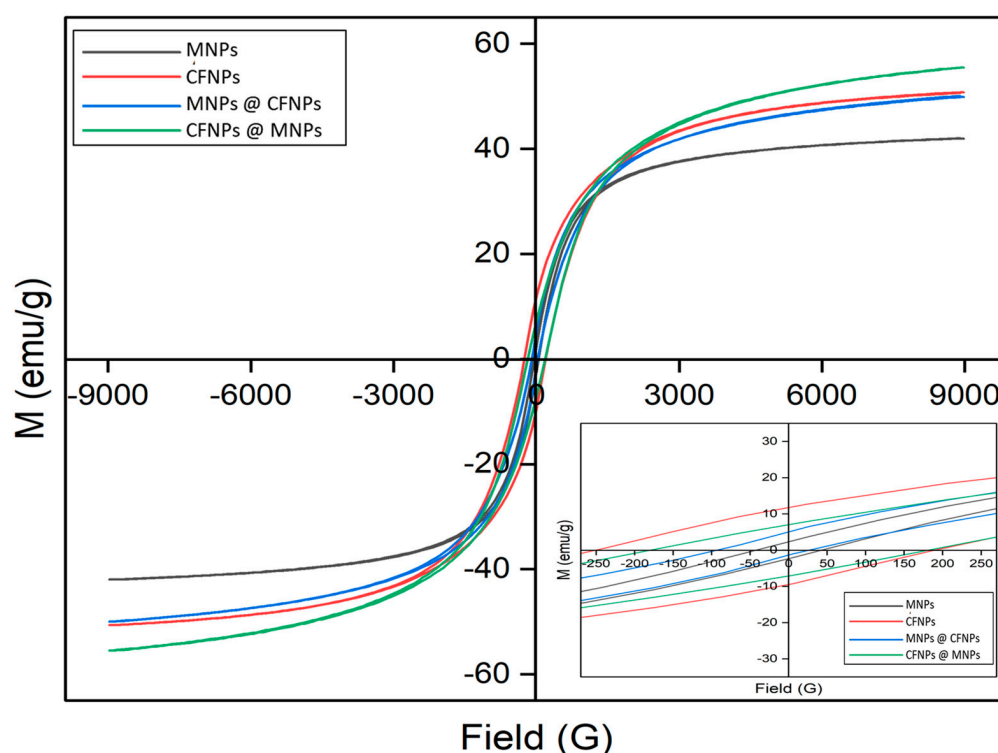


**Figure 5.** Magnetic properties of MNPs, CFNPs, MNPs @ CFNPs, and CFNPs @ MNPs.

**Table 3.** Magnetic properties of the fabricated particles.

Properties	MNPs	CFNPs	MNPs @ CFNPs	CFNPs @ MNPs
$M_s$ ( $\text{emu g}^{-1}$ )	41.9	50.6	49.8	55.4
$M_r$ ( $\text{emu g}^{-1}$ )	3.4	10.7	3.8	5.0
$H_c$ (Oe)	40.5	159.8	35.0	155.0
SQ	0.08	0.21	0.07	0.09

### 3.4. Photo Performance of the Nanostructures

The absorbance spectra of the materials were investigated via UV–vis spectroscopy at ambient temperature and are shown in Figure 6. The absorption character in the visible region arises from the electronic charge of  $\text{Co}^{2+}$  and  $\text{Fe}^{3+}$  and its level of conduction. The absorption behavior of the particle indicated a wide range from 300 to 600 nm in the visible range, which is probably due to the d-orbital movement of  $\text{Fe}^{3+}$ . The absorption band was around 490 nm for  $\text{Fe}^{3+}$  in a tetrahedral coordination environment [42]. The  $\lambda_{\text{max}}$  was detected at 490 nm, emphasizing that ferrite is active in the visible region. A band gap ( $E_g$ ) was calculated from the absorption spectra. The electron can move from one band to

another band provided it has the least minimum energy required for the movement. To calculate the band gap,  $(\alpha h\nu)^2$  was plotted against ' $h\nu$ '. The band gap is concerned with the absorption coefficient ' $\alpha$ ' by the Tauc equation:

$$(\alpha h\nu)^n = (\text{absorption coefficient} \times \text{energy})^n = (2.303Ah\nu)^n \quad (2)$$

where A is a constant,  $h\nu$  is the photon energy, and  $n$  is a number ( $= 2$  for direct transition).

$$\text{Band gap energy } (E_g) = (hc)/\lambda \quad (3)$$

where  $h$  is Planck's constant ( $6.626 \times 10^{-34}$  Joules/s),  $c$  is the speed of light ( $3.0 \times 10^8$  m/s), and  $\lambda$  is the cut-off wavelength ( $E_g = 1240 \text{ eV nm}/\lambda$ ) (energy in eV).

The calculated band gap energies were 2.35, 2.50, 2.25, and 1.45 eV for MNPs, CFNPs, MNPs @ CFNPs, and CFNPs @ MNPs. In Figure 6, for the core nanoparticles MNPs and CFNPs, the value raised from 2.35 to 2.50 eV, as the size lowered from 10 to 8 nm. Also, the same observation was noticed for the nanostructures MNPs @ CFNPs and CFNPs @ MNPs. The band gap value decreased from 2.25 to 1.45 eV for MNPs @ CFNPs and CFNPs @ MNPs by an increase in size from 12 to 14 nm. The band gap was recorded with a reverse relationship to their size, as observed in an earlier report [43]. The lowest band gap value (1.4 eV) of CFNPs @ MNPs could also enhance and affect the photocatalytic activity of this structure by reducing the light irradiation required through the splitting reaction [44].

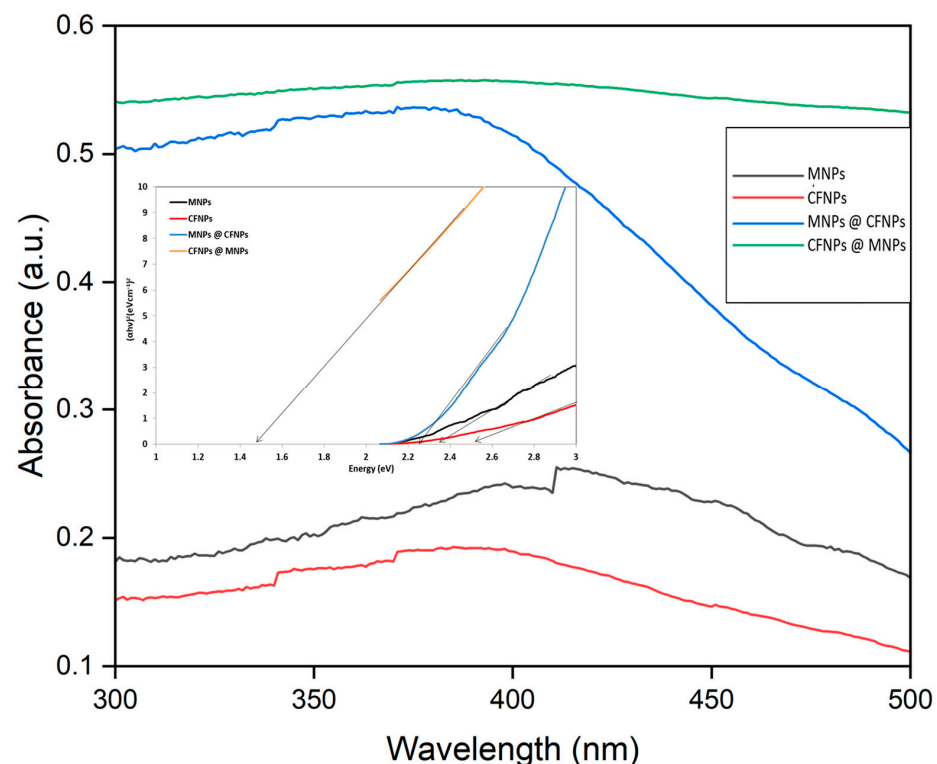


**Figure 6.** UV-Vis of MNPs, CFNPs, MNPs @ CFNPs, and CFNPs @ MNPs.

The photocatalytic activities of the prepared particles were studied for hydrogen production through the water-splitting process. The capability of iron oxide as a catalyst through the water-splitting reaction could be improved. So, the tune of layer composition could play an important part in the photocatalytic potential. During the photocatalytic process, the absorption of photons by the photocatalyst leads to the upgrading of an electron from the valence band to the conducting band, thus generating  $e^-h^+$  pairs. The proton's appearance is due to water or methanol oxidation via the radiation-produced holes [45,46]. The excited electron can reduce hydrogen ions, and the hole can oxidize

oxygen anions. Under magnetic force, the hydrogen yield was observed at 60, 26, 3.8, and 93 mmole min<sup>-1</sup> g<sup>-1</sup> for MNPs, CFNPs, MNPs @ CFNPs, and CFNPs @ MNPs (Figure 7).

The highest magnetic value of CFNPs @ MNPs could affect the photocatalytic property of this structure by minimizing the scattering of light irradiation within the splitting reaction (Figure 7). The yield using CFNPs @ MNPs was 1.5-fold higher than MNPs. Also, the yield using CFNPs @ MNPs was 24-fold higher than reversal MNPs @ CFNPs. This may be attributed to the better redox property of nano-ferrites, where the high hydrogen yield is due to the photocatalytic and thermochemical splitting of water. The yield was nearly naught in the absence of light and the photocatalyst. The highest Co % was detected at 8.48% for CFNPs @ MNPs, which is predicted to influence their behavior. The cobalt-based photocatalyst acts as an efficient collector that can harvest light and act as an electron mediator for effective charge transfer in photocatalytic hydrogen production. The lowest hydrogen yield was detected for MNPs @ CFNPs. It could be by the formation of an iron oxide amorphous layer or by partial core nanoparticle dissolution. It was reported that the morphology and crystalline properties of semiconductor nanoparticles have considerable influences on their photocatalytic activity [47,48]. The photocatalytic property and saturation magnetization of the magnetic TiO<sub>2</sub>/SrFe<sub>12</sub>O<sub>19</sub> photocatalyst could be tuned by altering the shell thickness [49].

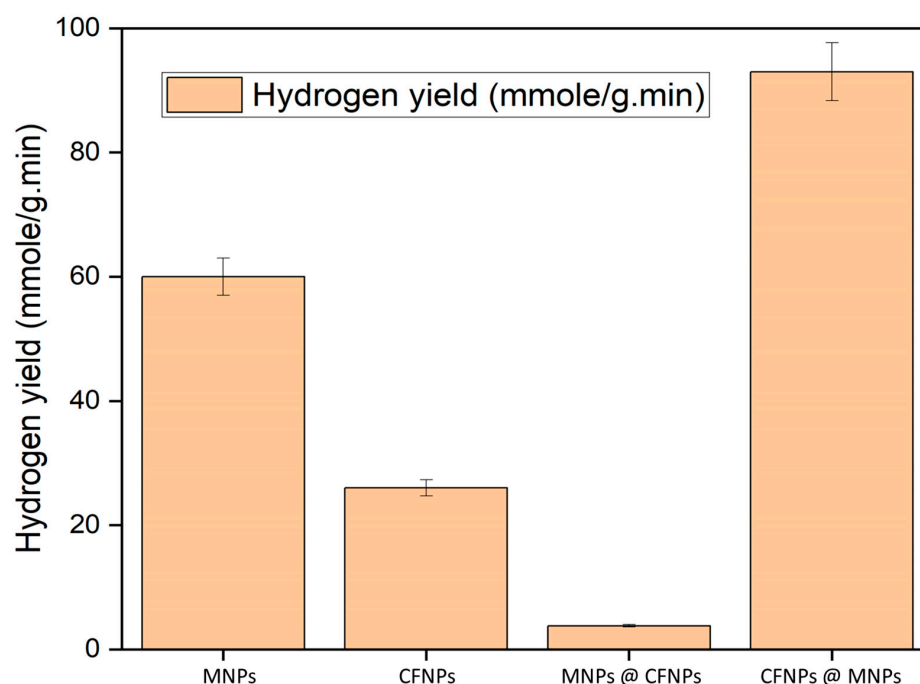


**Figure 7.** The yield using MNPs, CFNPs, MNPs @ CFNPs, and CFNPs @ MNPs.

Magnetic force could enhance the photocatalytic mechanism by raising carrier movement and increasing the mass transfer rate of ions in the system [50–59]. Under magnetic forces, this can defeat the charge recollection of ZnFe<sub>2</sub>O<sub>4</sub> because the electron spin polarization may be planned by magnetic force [52]. The magnetic force is proposed to assist in the photocatalytic mechanism since it could beneficially promote the separation of photo-generated charges without complex circuit systems [52,53]. Currently, it is known that there are two principal mechanisms of magnetic-assisted photocatalysis, Lorentz force and micro-electric potential [54,55]. Using a catalyst with solar energy for hydrogen production from water is one of the best outlets for clean and renewable energy. CFNPs @ MNPs displayed superior photocatalytic performance towards hydrogen yield, being a convenient photocatalysis in the water-splitting reaction. Increasing the yield could potentially be influenced by the magnetic behaviors of those nanoparticles during the splitting process under magnetic forces. Consequently, scattered radiation amounts could be minimized among the

photocatalyst particles during the splitting reactions [59]. Therefore, the magnetic behavior of the nanoparticles could affect the spin polarization of the electronic system of the photocatalysts due to the influence of the magnetic force [50]. The electron's spin polarization could result in the promoted motion of the nanoparticles through the reaction. Hence, enhanced interactions between nanoparticles and the water molecules were undertaken.

#### 4. Conclusions

A series of photocatalysts based on bi-magnetic nanostructures were prepared using the coprecipitation method. CFNPs @ MNPs had the largest particle size (~14 nm), while CFNPs had the smallest (~8 nm). CFNPs @ MNPs showed the highest  $M_s$  with a low  $M_r$  at 55.4 and 5.0 emu  $g^{-1}$ , respectively. The highest hydrogen yield was 93 mmole  $min^{-1} g^{-1}$  for CFNPs @ MNPs. The yield using CFNPs @ MNPs was 1.5-fold higher than MNPs. Also, the yield using CFNPs @ MNPs was 24-fold higher over reversal MNPs @ CFNPs. The highest magnetization value of CFNPs @ MNPs could also enhance and affect the photocatalytic property of this structure by reducing the light irradiation scattering in the water-splitting system.

**Author Contributions:** Conceptualization, resources, supervision, writing—review & editing, H.A.; conceptualization, resources, supervision, writing—review & editing, M.M.K.; conceptualization, methodology, writing—original draft, M.S.A.D. All authors have read and agreed to the published version of the manuscript.

**Funding:** This research received no external funding.

**Data Availability Statement:** The data is contained within the article.

**Conflicts of Interest:** The authors declare no conflict of interest.

#### References

1. Preethi, V.; Kanmani, S. Photocatalytic hydrogen production using  $Fe_2O_3$ -based core shell nano particles with ZnS and CdS. *Int. J. Hydrogen Energy* **2014**, *39*, 1613–1622. [[CrossRef](#)]
2. Madhumitha, A.; Preethi, V.; Kanmani, S. Photocatalytic hydrogen production using  $TiO_2$  coated iron-oxide core shell particles. *Int. J. Hydrogen Energy* **2018**, *43*, 3946–3956. [[CrossRef](#)]
3. Tian, F.Y.; Hou, D.; Tang, F.; Deng, M.; Qiao, X.Q.; Zhang, Q.; Wu, T.; Li, D.S. Novel  $Zn_{0.8}Cd_{0.2}S@g-C_3N_4$  core-shell heterojunctions with a twin structure for enhanced visible-light-driven photocatalytic hydrogen generation. *J. Mater. Chem. A* **2018**, *6*, 17086–17094.
4. Chang, C.J.; Lee, Z.; Wei, M.; Chang, C.C.; Chu, K.W. Photocatalytic hydrogen production by magnetically separable  $Fe_3O_4@ZnS$  and  $NiCo_2O_4@ZnS$  core-shell nanoparticles. *Int. J. Hydrogen Energy* **2015**, *40*, 11436–11443. [[CrossRef](#)]
5. Ye, Y.; Al-Khaledi, N.; Barker, L.; Darwish, M.S.; El Naggar, A.M.; El-Yahyaoui, A.; Hussein, A.; Hussein, E.S.; Shang, D.; Taha, M.; et al. Uranium resources in China's phosphate rocks—Identifying low-hanging fruits. *IOP Conf. Ser. Earth Environ. Sci.* **2019**, *227*, 052033. [[CrossRef](#)]
6. Motawie, M.; Hanafi, S.A.; Elmelawy, M.S.; Ahmed, S.M.; Mansour, N.A.; Darwish, M.S.; Abulyazied, D.E. Wax co-cracking synergism of high density polyethylene to alternative fuels. *Egypt. J. Pet.* **2015**, *24*, 353–361. [[CrossRef](#)]
7. Darwish, M.S.A.; Kunz, U.; Peuker, U. Preparation and catalytic use of platinum in magnetic core/shell nanocomposites. *J. Appl. Polym. Sci.* **2013**, *129*, 1806–1811. [[CrossRef](#)]
8. Patil, S.P.; Jagadale, S.A. Ferrites for electrocatalytic water splitting applications. In *Spinel Ferrite Nanostructures for Energy Storage Devices*; Elsevier: Amsterdam, The Netherlands, 2020; pp. 123–145.
9. Darwish, M.S.A.; Bakry, A.; Al-Harbi, L.; Khowdiary, M.; El-Henawy, A.; Yoon, J. Core/shell  $PA6@Fe_3O_4$  nanofibers: Magnetic and shielding behavior. *J. Dispers. Sci. Technol.* **2020**, *41*, 1711–1719. [[CrossRef](#)]
10. Saghafi, M.; Hosseini, S.A.; Zangeneh, S.; Moghanian, A.H.; Salarvand, V.; Vahedi, S.; Mohajerzadeh, S. Charge storage properties of mixed ternary transition metal ferrites  $MZnFe$  oxides ( $M = Al, Mg, Cu, Fe, Ni$ ) prepared by hydrothermal method. *SN Appl. Sci.* **2019**, *1*, 1303. [[CrossRef](#)]
11. Darwish, M.S.A.; El-Sabbagh, A.; Stibor, I. Hyperthermia properties of magnetic polyethylenimine core/shell nanoparticles: Influence of carrier and magnetic strength. *J. Polym. Res.* **2015**, *22*, 239. [[CrossRef](#)]
12. Bhagwat, V.R.; Humbe, A.V.; More, S.D.; Jadhav, K.M. Sol-gel auto combustion synthesis and characterizations of cobalt ferrite nanoparticles: Different fuels approach. *Mater. Sci. Eng. B* **2019**, *248*, 114388. [[CrossRef](#)]
13. Abbasi, L.; Hedayati, K.; Ghanbari, D. Magnetic properties and kinetic roughening study of prepared polyaniline: Lead ferrite, cobalt ferrite and nickel ferrite nanocomposites electrodeposited thin films. *J. Mater. Sci. Mater. Electron.* **2021**, *32*, 14477e93. [[CrossRef](#)]

14. Skoropata, E.; Desautels, R.D.; Chi, C.C.; Ouyang, H.; Freeland, J.W.; van Lierop, J. Magnetism of iron oxide based core-shell nanoparticles from interface mixing with enhanced spin-orbit coupling. *Phys. Rev. B* **2014**, *89*, 024410. [[CrossRef](#)]
15. López-Ortega, A.; Estrader, M.; Salazar-Alvarez, G.; Roca, A.G.; Nogués, J. Applications of exchange coupled bi-magnetic hard/soft and soft/hard magnetic core/shell nanoparticles. *Phys. Rep.* **2015**, *553*, 1–32. [[CrossRef](#)]
16. Mangrulkar, P.A.; Joshi, M.M.; Tijare, S.N.; Polshettiwar, V.; Labhsetwar, N.K.; Rayalu, S.S. Nano cobalt oxides for photocatalytic hydrogen production. *Int. J. Hydrogen Energy* **2012**, *37*, 10462–10466. [[CrossRef](#)]
17. Demortière, A.; Panissod, P.; Pichon, B.P.; Pourroy, G.; Guillon, D.; Donnio, B.; Bégin-Colin, S. Size-dependent properties of magnetic iron oxide nanocrystals. *Nanoscale* **2011**, *3*, 225–232. [[CrossRef](#)]
18. Hosni, N.; Zehani, K.; Bartoli, T.; Bessais, L.; Maghraoui-Meherzi, H. Semi-hard magnetic properties of nanoparticles of cobalt ferrite synthesized by the co-precipitation process. *J. Alloys Compd.* **2017**, *694*, 1295–1301. [[CrossRef](#)]
19. Ibrahim, I.; Belessiotis, G.; Antoniadou, M.; Kaltzoglou, A.; Sakellis, E.; Katsaros, F.; Sygellou, L.; Arfanis, M.; Salama, T.; Falaras, P. Silver decorated TiO<sub>2</sub>/g-C<sub>3</sub>N<sub>4</sub> bifunctional nanocomposites for photocatalytic elimination of water pollutants under UV and artificial solar light. *Results Eng.* **2022**, *14*, 100470. [[CrossRef](#)]
20. Belessiotis, G.V.; Falara, P.P.; Ibrahim, I.; Kontos, A.G. Magnetic Metal Oxide-Based Photocatalysts with Integrated Silver for Water Treatment. *Materials* **2022**, *15*, 4629. [[CrossRef](#)] [[PubMed](#)]
21. Ibrahim, I.; Belessiotis, G.V.; Elseman, A.M.; Mohamed, M.M.; Ren, Y.; Salama, T.M.; Mohamed, M.B.I. Magnetic TiO<sub>2</sub>/CoFe<sub>2</sub>O<sub>4</sub> Photocatalysts for Degradation of Organic Dyes and Pharmaceuticals without Oxidants. *Nanomaterials* **2022**, *12*, 3290. [[CrossRef](#)]
22. Falara, P.P.; Ibrahim, I.; Zourou, A.; Sygellou, L.; Sanchez, D.E.; Romanos, G.E.; Givalou, L.; Antoniadou, M.; Arfanis, M.K.; Han, C.; et al. Bi-functional photocatalytic heterostructures combining titania thin films with carbon quantum dots (C-QDs/TiO<sub>2</sub>) for effective elimination of water pollutants. *Environ. Sci. Pollut. Res.* **2023**, 1–16. [[CrossRef](#)] [[PubMed](#)]
23. Marcuello, C.; Chambel, L.; Rodrigues, M.S.; Ferreira, L.P.; Cruz, M.M. Magnetotactic Bacteria: Magnetism Beyond Magnetosomes. *IEEE Trans. Nano Biosci.* **2018**, *17*, 555–559. [[CrossRef](#)] [[PubMed](#)]
24. Wang, Q.; Ma, X.; Liao, H.; Liang, Z.; Li, F.; Tian, J.; Ling, D. Artificially Engineered Cubic Iron Oxide Nanoparticle as a High-Performance Magnetic Particle Imaging Tracer for Stem Cell Tracking. *ACS Nano* **2020**, *14*, 2053–2062. [[CrossRef](#)]
25. Chen, X.; Shen, S.; Guo, L.; Mao, S.S. Semiconductor-based photocatalytic hydrogen generation. *Chem. Rev.* **2010**, *110*, 6503–6570. [[CrossRef](#)]
26. Chen, X.; Li, C.; Grätzel, M.; Kostecki, R.; Mao, S.S. Nanomaterials for renewable energy production and storage. *Chem. Soc. Rev.* **2012**, *41*, 7909–7937. [[CrossRef](#)]
27. Artero, V.; Chavarot-Kerlidou, M.; Fontecave, M. Splitting water with cobalt. *Angew. Chem. Int. Ed.* **2011**, *50*, 7238–7266. [[CrossRef](#)] [[PubMed](#)]
28. An, W.-J.; Wang, W.-N.; Ramalingam, B.; Mukherjee, S.; Daubayev, B.; Gangopadhyay, S.; Biswas, P. Enhanced water photolysis with Pt metal nanoparticles on single crystal TiO<sub>2</sub> surfaces. *Langmuir* **2012**, *28*, 7528–7534. [[CrossRef](#)]
29. Jang, J.S.; Choi, S.H.; Kim, D.H.; Jang, J.W.; Lee, K.S.; Lee, J.S. Enhanced photocatalytic hydrogen production from water-methanol solution by nickel intercalated into titanate nanotube. *J. Phys. Chem. C* **2009**, *113*, 8990–8996. [[CrossRef](#)]
30. Nasrin, S.; Chowdhury, F.U.Z.; Hoque, S.M. Study of hyperthermia temperature of manganese-substituted cobalt nano ferrites prepared by chemical co-precipitation method for biomedical application. *J. Magn. Magn. Mater.* **2019**, *479*, 126–134. [[CrossRef](#)]
31. Darwish, M.S.A. Magnetite@Zinc Cobalt Ferrite Nanoparticles: Synthesis, Magnetic Behavior, and Optical Properties. *Crystals* **2023**, *13*, 1284. [[CrossRef](#)]
32. Badawy, S.M.; Abd, E.-L. Synthesis and characterizations of magnetite nanocomposite films for radiation shielding. *Polym. Compos.* **2017**, *38*, 974–980. [[CrossRef](#)]
33. Kmita, A.; Lachowicz, D.; Zukrowski, J.; Gajewska, M.; Szczerba, W.; Kuciakowski, J.; Zapotoczny, S.; Sikora, M. One-step synthesis of long term stable superparamagnetic colloid of zinc ferrite nanorods in water. *Materials* **2019**, *12*, 1048. [[CrossRef](#)] [[PubMed](#)]
34. Darwish, M.S.A.; Stibor, I. Pentenoic acid-stabilized magnetic nanoparticles for nanomedicine applications. *J. Dispers. Sci. Technol.* **2016**, *37*, 1793–1798. [[CrossRef](#)]
35. Škrátek, M.; Dvurečenskij, A.; Kluknavský, M.; Barta, A.; Bališ, P.; Mičurová, A.; Cigáň, A.; Eckstein-Andicsová, A.; Maňka, J.; Bernátová, I. Sensitive SQUID Bio-Magnetometry for Determination and Differentiation of Biogenic Iron and Iron Oxide Nanoparticles in the Biological Samples. *Nanomaterials* **2020**, *10*, 1993. [[CrossRef](#)]
36. Winkler, R.; Ciria, M.; Ahmad, M.; Plank, H.; Marcuello, C. A Review of the Current State of Magnetic Force Microscopy to Unravel the Magnetic Properties of Nanomaterials Applied in Biological Systems and Future Directions for Quantum Technologies. *Nanomaterials* **2023**, *13*, 2585. [[CrossRef](#)]
37. Choi, H.; An, M.; Eom, W.; Lim, S.; Shim, I.; Kim, C.; Kim, S.J. Crystallographic and magnetic properties of the hyperthermia material CoFe<sub>2</sub>O<sub>4</sub>@AlFe<sub>2</sub>O<sub>4</sub>. *Korean Phys. Soc.* **2017**, *70*, 173–176. [[CrossRef](#)]
38. Obaidat, I.M.; Issa, B.; Haik, Y. Magnetic properties of magnetic nanoparticles for efficient hyperthermia. *Nanomaterials* **2015**, *5*, 63–89. [[CrossRef](#)]
39. Zhen, G.B.; Muir, W.; Moffat, B.A.; Harbour, P.; Murray, K.S.; Moubaraki, B.; Suzuki, K.; Madsen, I.; Agron-Olshina, N.; Waddington, L.; et al. Comparative study of the magnetic behavior of spherical and cubic superparamagnetic iron oxide nanoparticles. *J. Phys. Chem. C* **2011**, *115*, 327–334. [[CrossRef](#)]

40. Pereira, C.; Pereira, A.M.; Fernandes, C.; Rocha, M.; Mendes, R.; Fernández-García, M.P.; Guedes, A.; Tavares, P.B.; Grenèche, J.M.; Araújo, J.P.; et al. Superparamagnetic  $MFe_2O_4$  ( $M = Fe, Co, Mn$ ) nanoparticles: Tuning the particle size and magnetic properties through a novel one-step coprecipitation route. *Chem. Mater.* **2012**, *24*, 1496–1504. [[CrossRef](#)]
41. Song, Q.; Zhang, Z.J. Controlled synthesis and magnetic properties of bimagnetic spinel ferrite  $CoFe_2O_4$  and  $MnFe_2O_4$  nanocrystals with core-shell architecture. *J. Am. Chem. Soc.* **2012**, *134*, 10182–10190. [[CrossRef](#)]
42. Mallick, P.; Dash, B.N. X-ray diffraction and UV-Visible characterizations of  $\gamma-Fe_2O_3$  nanoparticles annealed at different temperature. *Nanosci. Nanotechnol.* **2013**, *3*, 130–134.
43. Anjum, S.; Tufail, R.; Rashid, K.; Zia, R.; Riaz, S. Effect of cobalt doping on crystallinity, stability, magnetic and optical properties of magnetic iron oxide nano-particles. *J. Magn. Magn. Mater.* **2017**, *432*, 198–207. [[CrossRef](#)]
44. Wender, H.; Gonçalves, R.V.; Dias, C.S.B.; Zapata, M.J.M.; Zagonel, L.F.; Mendonça, E.C.; Sérgio, R. Teixeira and Flávio Garcia Photocatalytic hydrogen production of  $Co(OH)_2$  nanoparticle-coated  $\alpha-Fe_2O_3$  nanorings. *Nanoscale* **2013**, *5*, 9310–9316. [[CrossRef](#)] [[PubMed](#)]
45. Choi, H.-J.; Kang, M. Hydrogen production from methanol-water decomposition in a liquid photosystem using the anatase structure of Cu loaded  $TiO_2$ . *Int. J. Hydrogen Energy* **2007**, *32*, 3841–3848. [[CrossRef](#)]
46. Chen, J.; Ollis, D.F.; Rulken, W.H.; Bruning, H. Photocatalyzed oxidation of alcohols and organochlorides in the presence of native  $TiO_2$  and metallized  $TiO_2$  suspensions. Part (II): Photocatalytic mechanisms. *Water Res.* **1999**, *33*, 669–676. [[CrossRef](#)]
47. Fang, D.; Luo, Z.; Huang, K.; Lagoudas, D.C. Effect of heat treatment on morphology, crystalline structure and photocatalysis properties of  $TiO_2$  nanotubes on Ti substrate and freestanding membrane. *Appl. Surf. Sci.* **2011**, *257*, 6451–6461. [[CrossRef](#)]
48. Hung, S.T.; Chang, C.J.; Hsu, C.H.; Chu, B.H.; Lo, C.F.; Hsu, C.C.; Pearton, S.J.; Holzworth, M.R.; Whiting, P.G.; Rudawski, N.G.; et al.  $SnO_2$  functionalized  $AlGaIn/GaN$  high electron mobility transistor for hydrogen sensing applications. *Int. J. Hydrogen Energy* **2012**, *37*, 13783–13788. [[CrossRef](#)]
49. Fu, W.; Yang, H.; Chang, L.; Bala, H.; Li, M.; Zou, G. Anatase  $TiO_2$  nanolayer coating on strontium ferrite nanoparticles for magnetic photocatalyst. *Colloids Surf. A Physicochem. Eng. Asp.* **2006**, *289*, 47–52. [[CrossRef](#)]
50. Garcés-Pineda, F.A.; Blasco-Ahicart, M.; Nieto-Castro, D.; López, N.; GalánMascarós, J.R. Direct magnetic enhancement of electrocatalytic water oxidation in alkaline media. *Nat. Energy* **2019**, *4*, 519–525. [[CrossRef](#)]
51. Huang, H.J.; Wang, Y.H.; Chau, Y.F.C.; Chiang, H.P.; Wu, J.C.S. Magnetic Field-Enhancing Photocatalytic Reaction in Micro Optofluidic Chip Reactor. *Nanoscale Res. Lett.* **2019**, *14*, 323. [[CrossRef](#)]
52. Gao, W.; Peng, R.; Yang, Y.; Zhao, X.; Cui, C.; Su, X.; Qin, W.; Dai, Y.; Ma, Y.; Liu, H.; et al. Electron Spin Polarization-Enhanced Photoinduced Charge Separation in Ferromagnetic  $ZnFe_2O_4$ . *ACS Energy Lett.* **2021**, *6*, 2129–2137. [[CrossRef](#)]
53. Li, J.; Pei, Q.; Wang, R.Y.; Zhou, Y.; Zhang, Z.M.; Cao, Q.Q.; Wang, D.H.; Mi, W.B.; Du, Y.W. Enhanced photocatalytic performance through magnetic field boosting carrier transport. *ACS Nano* **2018**, *12*, 3351–3359. [[CrossRef](#)] [[PubMed](#)]
54. Li, J.; Yin, W.; Pan, J.; Zhang, Y.; Wang, F.; Wang, L.; Zhao, Q. External field assisted hydrogen evolution reaction. *Nano Res.* **2023**, *16*, 8638–8654. [[CrossRef](#)]
55. Li, H.D.; Sang, Y.H.; Chang, S.J.; Huang, X.; Zhang, Y.; Yang, R.S.; Jiang, H.D.; Liu, H.; Wang, Z.L. Enhanced ferroelectric-nanocrystalbased hybrid photocatalysis by ultrasonic-wavegenerated piezophototronic effect. *Nano Lett.* **2015**, *15*, 2372–2379. [[CrossRef](#)]
56. Shi, Q.J.; Zhang, M.; Zhang, Z.M.; Li, Y.X.; Qu, Y.; Liu, Z.Q.; Yang, J.L.; Xie, M.Z.; Han, W.H. Energy and separation optimization of photogenerated charge in  $BiVO_4$  quantum dots by piezo-potential for efficient gaseous pollutant degradation. *Nano Energy* **2020**, *69*, 104448. [[CrossRef](#)]
57. Gao, W.Q.; Lu, J.B.; Zhang, S.; Zhang, X.F.; Wang, Z.X.; Qin, W.; Wang, J.J.; Zhou, W.J.; Liu, H.; Sang, Y.H. Suppressing photoinduced charge recombination via the Lorentz force in a photocatalytic system. *Adv. Sci.* **2019**, *6*, 1901244. [[CrossRef](#)] [[PubMed](#)]
58. Gao, W.Q.; Liu, Q.L.; Zhang, S.; Yang, Y.Y.; Zhang, X.F.; Zhao, H.; Qin, W.; Zhou, W.J.; Wang, X.N.; Liu, H.; et al. Electromagnetic induction derived micro-electric potential in metalsemiconductor core-shell hybrid nanostructure enhancing charge separation for high performance photocatalysis. *Nano Energy* **2020**, *71*, 104624. [[CrossRef](#)]
59. Darwish, M.S.; El Naggar, A.M.; Morshedy, A.S.; Haneklaus, N. Increased production of hydrogen with in situ  $CO_2$  capture through the process of water splitting using magnetic core/shell structures as novel photocatalysts. *Environ. Sci. Pollut. Res.* **2021**, *28*, 3566–3578. [[CrossRef](#)]

**Disclaimer/Publisher’s Note:** The statements, opinions and data contained in all publications are solely those of the individual author(s) and contributor(s) and not of MDPI and/or the editor(s). MDPI and/or the editor(s) disclaim responsibility for any injury to people or property resulting from any ideas, methods, instructions or products referred to in the content.